iScience

CellPress

Article

Bundled Three-Dimensional Human Axon Tracts Derived from Brain Organoids

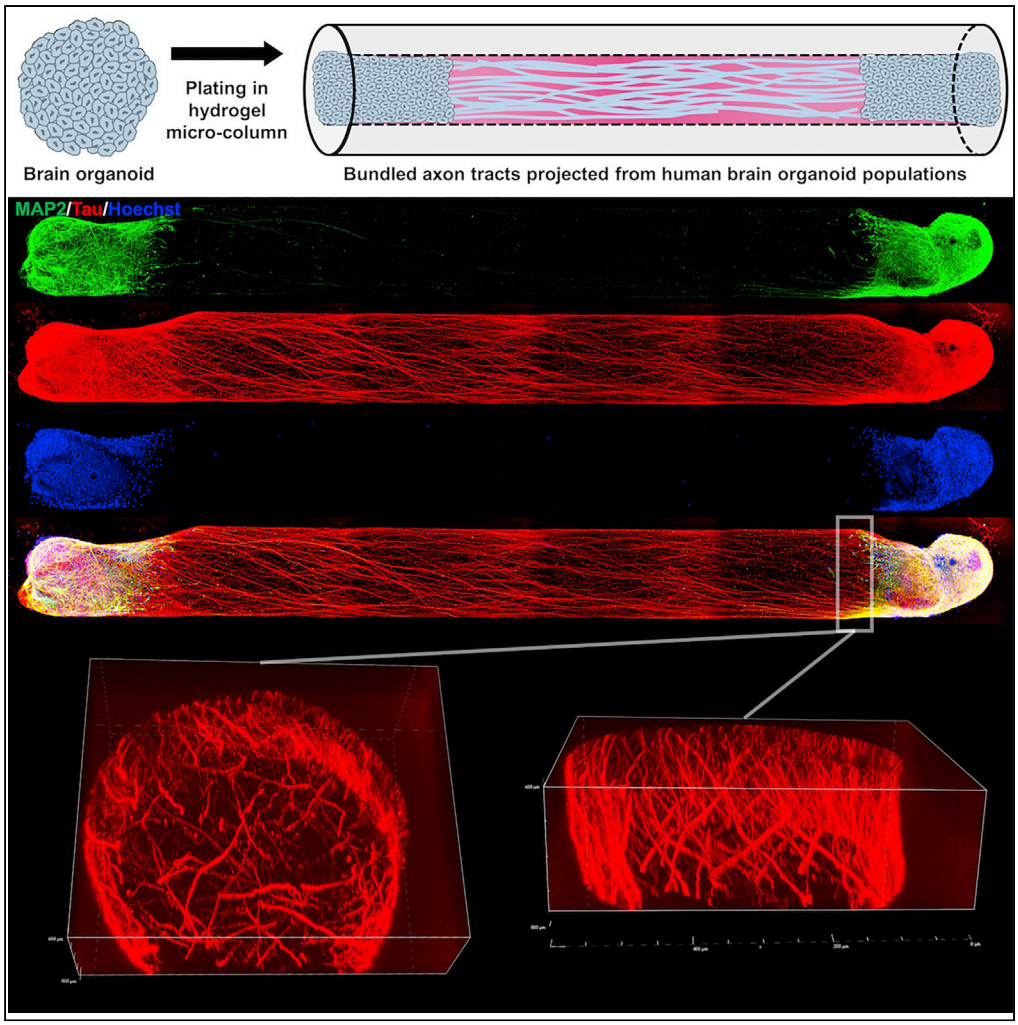

D. Kacy Cullen, Wisberty J. Gordián-Vélez, Laura A. Struzyna, ..., Kathryn L. Wofford, Kevin D. Browne, H. Isaac Chen

dkacy@pennmedicine.upenn.edu (D.K.C.)
isaac.chen@uphs.upenn.edu (H.I.C.)

HIGHLIGHTS

Transplantable 3D axon tracts are tissue engineered from human brain organoids

Growth of organoid axons in a hydrogel column is enhanced compared with planar culture

Organoids within engineered columns can maintain a laminar cortical architecture

Functional connectivity across the construct is demonstrated using calcium imaging

Cullen et al., iScience *21*, 57–67
November 22, 2019
https://doi.org/10.1016/j.isci.2019.10.004

iScience

CellPress

Article

Bundled Three-Dimensional Human Axon Tracts Derived from Brain Organoids

D. Kacy Cullen,[1,2,3,*] Wisberty J. Gordián-Vélez,[1,2,3] Laura A. Struzyna,[1,2,3] Dennis Jgamadze,[1,2] James Lim,[1,2] Kathryn L. Wofford,[1,2] Kevin D. Browne,[1,2] and H. Isaac Chen[1,2,4,*]

SUMMARY

Reestablishing cerebral connectivity is a critical part of restoring neuronal network integrity and brain function after trauma, stroke, and neurodegenerative diseases. Creating transplantable axon tracts in the laboratory is an unexplored strategy for overcoming the common barriers limiting axon regeneration *in vivo*, including growth-inhibiting factors and the limited outgrowth capacity of mature neurons in the brain. We describe the generation, phenotype, and connectivity of constrained three-dimensional human axon tracts derived from brain organoids. These centimeter-long constructs are encased in an agarose shell that permits physical manipulation and are composed of discrete cellular regions spanned by axon tracts, mirroring the separation of cerebral gray and white matter. Features of cerebral cortex also are emulated, as evidenced by the presence of neurons with different cortical layer phenotypes. This engineered neural tissue represents a first step toward potentially reconstructing brain circuits by physically replacing neuronal populations and long-range axon tracts in the brain.

INTRODUCTION

Recent advances in understanding the brain from a network perspective (Bassett et al., 2017) suggest that restoring connectivity among different regions of the brain after cerebral injury is crucial for recovering function. However, axon regeneration in the central nervous system is severely restricted after traumatic brain injury, stroke, and other similar conditions because of the presence of environmental axon growth inhibitors (Yiu and He, 2006) and the limited regenerative potential of mature neurons (Fernandes et al., 1999; He and Jin, 2016). Moreover, although intrinsic plasticity mechanisms exist in the brain (Chen et al., 2014), the extent to which the brain can rewire itself is constrained, especially in cases of extensive brain damage. There is thus a critical need to develop strategies for reconstructing brain circuitry.

Prior approaches for restoring axonal pathways include dampening the effects of axon growth inhibitors (GrandPre et al., 2002; Wiessner et al., 2003), augmenting intrinsic neuronal growth programs (Sun et al., 2011), providing pathways that facilitate axon growth (David and Aguayo, 1981; Martinez-Ramos et al., 2012), and adding new neural elements capable of extending processes (Espuny-Camacho et al., 2013; Gaillard et al., 2007). These strategies are all based on the fundamental concept of promoting axon growth *in vivo*. A different approach is the transplantation of preformed axon tracts that are engineered *in vitro*. This alternative relies upon graft integration via the formation of local synaptic connections between transplanted neurons and the host brain but dispenses with the need for long-range axon regeneration. Other benefits include a greater degree of control over a broader array of available tools for promoting axon growth (Chen et al., 2016). Available technologies for axon engineering include stretch growth (Chen et al., 2019; Pfister et al., 2004), patterned substrates (Pan et al., 2015; Smith et al., 1999), and hydrogel micro-columns (Cullen et al., 2012; Struzyna et al., 2015b). Thus far, these methods have utilized primarily dissociated neuronal cultures.

Brain organoids are neural tissues derived from the self-organization of pluripotent stem cells (Kadoshima et al., 2013; Lancaster et al., 2013; Pasca et al., 2015; Qian et al., 2016). They develop a significant degree of brain architecture, including rudimentary cortical layers, but large-scale axon bundles are not seen. Inducing the growth of axons from organoids in a controlled manner could lead to repair candidates that replace not only white matter pathways but also gray matter structure (Figure 1A). Here, we combined brain organoids with hydrogel micro-columns to generate centimeter-long human axon tracts in a three-dimensional (3D), transplantable format. We report the growth characteristics of axons in these constructs, the phenotype and structure of the axonal and somatic regions, and an initial assessment of anatomic and functional connectivity.

[1]Center for Brain Injury & Repair, Department of Neurosurgery, Perelman School of Medicine, University of Pennsylvania, 105E Hayden Hall/3320 Smith Walk, 3rd Floor, Silverstein Pavilion/3400 Spruce Street, Philadelphia, PA 19104, USA

[2]Center for Neurotrauma, Neurodegeneration & Restoration, Corporal Michael J. Crescenz Veterans Affairs Medical Center, Philadelphia, PA 19104, USA

[3]Department of Bioengineering, School of Engineering and Applied Science, University of Pennsylvania, Philadelphia, PA 19104, USA

[4]Lead Contact

*Correspondence: dkacy@pennmedicine.upenn.edu (D.K.C.), isaac.chen@uphs.upenn.edu (H.I.C.)

https://doi.org/10.1016/j.isci.2019.10.004

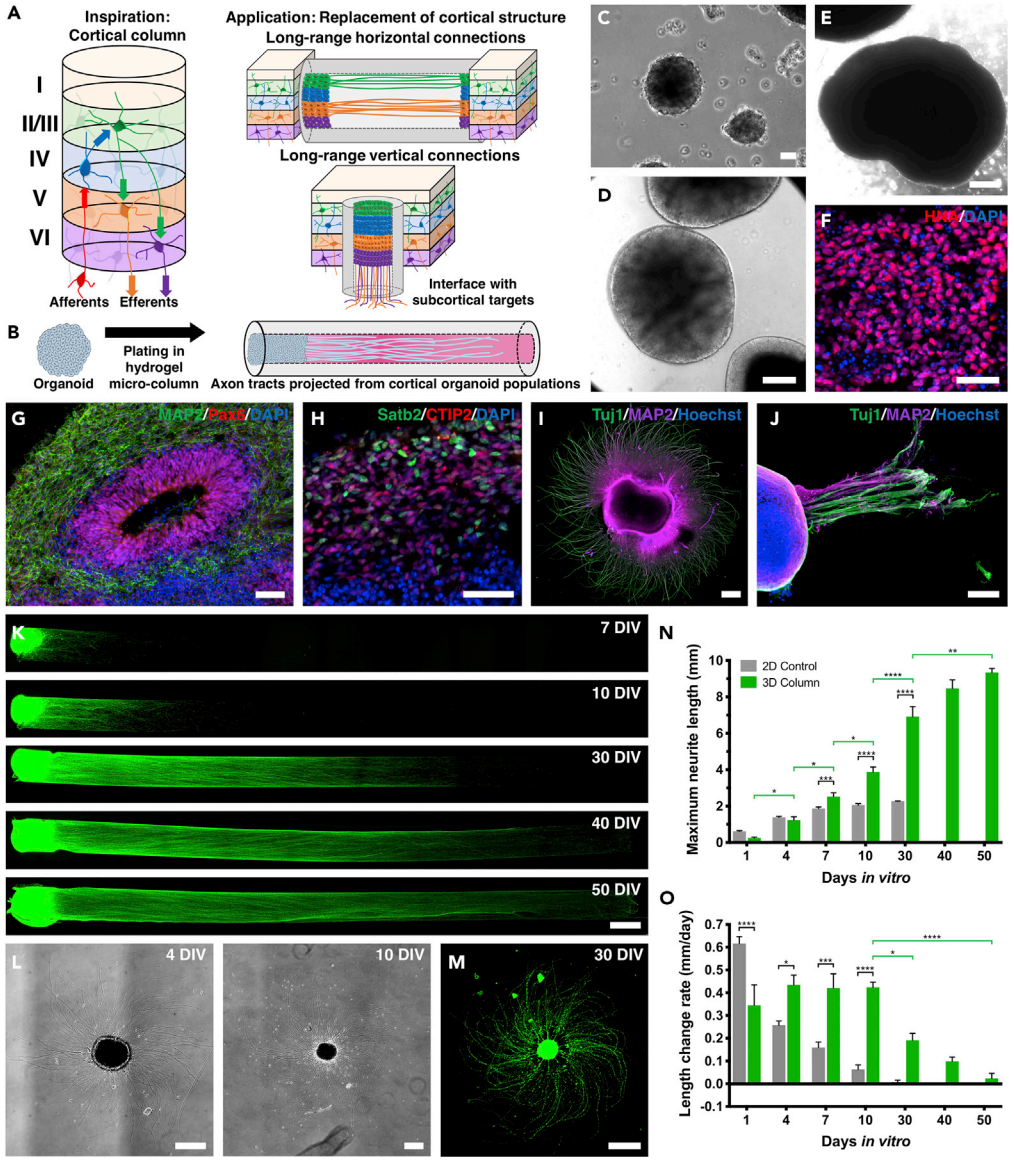

Figure 1. Organoid μTENN Generation and Unidirectional Neurite Growth Characterization

(A) Cerebral cortex has a stereotyped laminar architecture and micro-circuitry (left). In brief, thalamic inputs enter layer IV, which transmits information to layers II and III. Processed data are then conveyed from these layers to layers V and VI, which send outputs to subcortical targets. Horizontal projections exist primarily in layers II/III and V. Engineered cortical tissue/axons could serve as replacements for both long-range horizontal and vertical connections (right).

(B–E) (B) Human embryonic and induced pluripotent stem cell lines were used to generate brain organoids using a modified version of existing protocols (Pasca et al., 2015). Organoids were inserted into one or both ends of the μTENN micro-column. The micro-column lumen provided the necessary directionality for the formation of aligned neurite tracts. Phase contrast micrographs show embryoid bodies (C) and dd15 (D) and dd45 brain organoids (E).

(F) Immunofluorescence staining confirmed the human origin of these organoids (human nuclear antigen, red).

(G) Organoids (dd61) recapitulated neurodevelopmental structures, including ventricle-like zones surrounded by neural progenitors (Pax6, red) and differentiated neurons (MAP2, green).

(H) Separation of upper- (Satb2, green) and lower-layer (CTIP2, red) cortical neurons also was observed (dd61).

(I) Organoids plated on a planar surface extend neurites in an isotropic manner (MAP2, magenta; Tuj1, green; Hoechst, blue).

(J) In contrast, organoids inserted into a μTENN micro-column displayed directional growth of neurites within the lumen, as shown by this image of an ESC-derived construct that had extruded from the agarose outer shell (25 DIV; MAP2, magenta; Tuj1, green; Hoechst, blue).

Figure 1. *Continued*

(K–M) (K) Confocal images of GFP+ iPSC-derived organoid μTENNs in 1-cm columns were obtained at multiple time points up to 50 DIV. These images show that organoids can support the growth of long, aligned neurites spanning a width of 500 μm and extending up to ~1 cm at 50 DIV. Phase contrast (L) and confocal images (M, GFP) show an organoid grown on laminin-coated planar surfaces as a control.

(N) The length of neurite growth was quantified as a function of time for organoids grown in 3D micro-columns and on planar surfaces. By 7 DIV, neurite length in the 3D micro-columns was significantly greater than that on planar surfaces, with the former eventually reaching lengths close to 1 cm, whereas the latter plateaued at 2 mm.

(O) Neurite growth rates declined over time in both conditions but were maintained at higher levels in the micro-column condition.

Data are presented as mean ± SEM (*$p < 0.05$, **$p < 0.01$, ***$p < 0.001$, ****$p < 0.0001$; Tukey's multiple comparisons test). Scale bars: 500 μm (C, E, I, K, and M), 200 μm (D), 40 μm (F), 100 μm (G), 50 μm (H), 150 μm (J), and 250 μm (L).

RESULTS

Generation of Organoid μTENNs

Micro-tissue engineered neural networks (μTENNs) are hydrogel columns that are hundreds of microns in diameter and patterned to separate neuronal somata from aligned neurites (Cullen et al., 2012; Struzyna et al., 2015a). This configuration recreates, in part, the segregation of neuronal populations and long-range axon tracts found in the brain. These constructs consist of a relatively firm hydrogel shell that can withstand physical manipulation and an extracellular matrix core conducive to cellular and neurite growth (Figure 1B). In the present study, we engineered agarose tubes containing a cross-linked type I collagen core that facilitated the constrained growth of neurites.

Cortical organoids were generated from both the H9 human embryonic stem cell (ESC) and a human induced pluripotent stem (iPSC) line from a healthy volunteer using a modified version of a previously published protocol (Pasca et al., 2015). Embryoid bodies derived from enzymatic elevation of whole pluripotent stem cell colonies (Figure 1C) developed into organoids with multiple internal substructures and peripheral translucency, a marker of developing neuroepithelium (Figures 1D and 1E). These organoids expressed human nuclear antigen (Figure 1F) and formed ventricle-like structures surrounded by an adjacent layer of neural progenitors (Pax6+) and an outer layer of differentiated neurons (MAP2) (Figure 1G). By differentiation day (dd) 61, both upper- (Satb2+) and lower-layer (CTIP2+) cortical neurons were identified with the development of rudimentary laminar architecture (Figure 1H). Organoids cultured on a planar surface extended neurites in an isotropic fashion (Figure 1I), whereas organoid tissue inserted into one end of a hydrogel micro-column projected a combination of axons (Tuj1+/MAP2-) and dendrites (Tuj1+/MAP2+) exclusively along the length of the collagen matrix core (Figure 1J).

Neurite Growth in Organoid μTENNs versus Non-manipulated Organoids

Taking advantage of this directional growth of organoid-derived neurites, we generated unidirectional organoid μTENNs (Figure 1K) and determined their neurite growth characteristics over 50 days *in vitro* (DIV). We observed progressive growth of these neurites until they reached the end of the 1-cm micro-column, which was seen as early as 40 DIV. Organoids grown on planar surfaces exhibited isotropic neurite growth over time (Figures 1L and 1M), but these neurites were qualitatively shorter and less dense than those seen in the 3D organoid μTENNs. To better compare neurite growth between 3D and planar growth conditions, we quantified neurite length (Figure 1N) and growth rates (Figure 1O) for each group at multiple time points. Neurites in the organoid μTENNs were significantly longer than those in the planar organoids from 7 DIV onward. Neurites from planar organoids plateaued in length at about 2 mm by 10 DIV, whereas neurites within the organoid μTENNs continued to grow until the end of the micro-column was approached. This difference was also captured in the growth rate analysis, which showed relatively stable neurite growth in the organoid μTENNs at ~0.4 mm/day for 10 DIV before a drop in growth rates. In contrast, planar organoids exhibited a steady decrease in growth rates from the start. To rule out cell viability as a potential reason for this difference in neurite growth, we evaluated the health of organoid μTENNs versus organoids that had not been placed in a micro-column using a live-dead stain. We found no difference in the proportion of live cells between the two groups at 30 or 60 DIV (Figure S1).

Neurite Segment Characterization of Bidirectional Organoid μTENNs

We next assessed the growth patterns and structural details of the neurites in bidirectional μTENNs, in which organoid tissue was inserted into both ends of the hydrogel micro-column. Initially, 0.5-cm constructs were generated (Figure S2A). At this construct length, neurites crossed the entire length of the

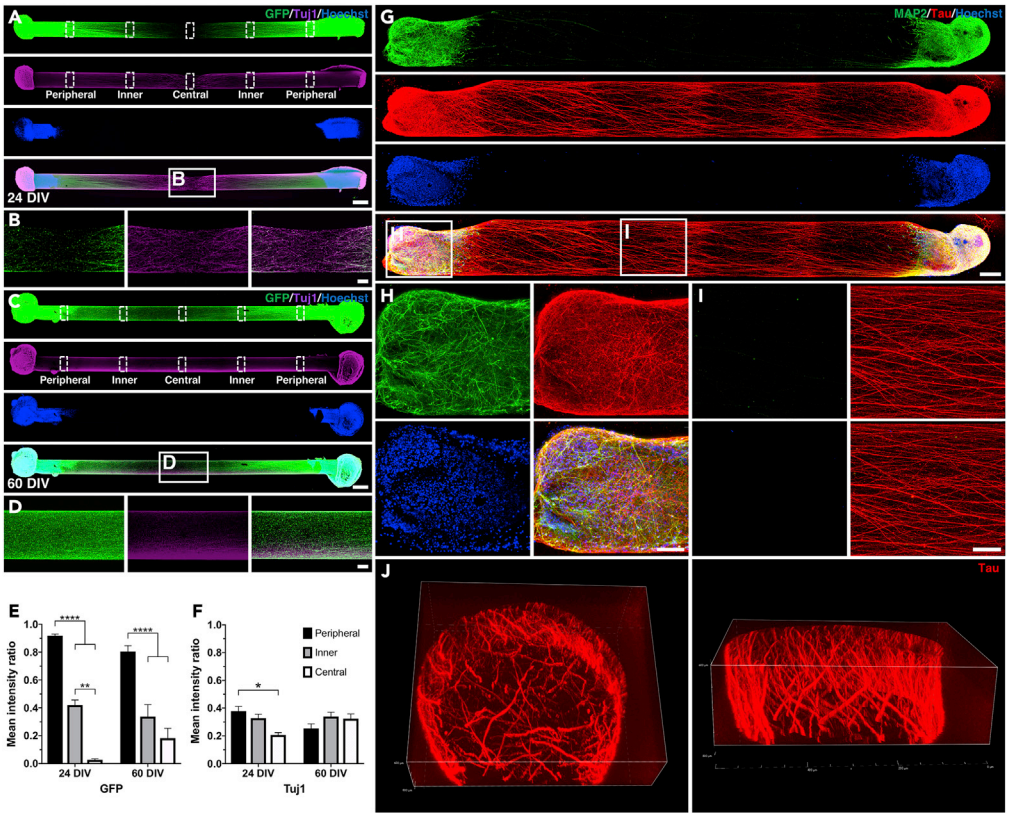

Figure 2. Phenotypic and Growth Characterization of Neurites in Bidirectional μTENNs

(A–F) Confocal reconstructions of 1-cm GFP+ ESC-derived constructs cultured for 24 (A) or 60 DIV (C) and stained for Tuj1 (magenta) and Hoechst (blue). Magnified images of the neurite tracts qualitatively show that neurites populate the center of the micro-column with a lesser density at 24 DIV (B) compared with 60 DIV (D). Quantification of the mean GFP (E) and Tuj1 (F) intensities in the different regions of interest in A and C confirm that neurites at the center of the μTENN reach a more homogeneous distribution at the later time point.

(G–I) (G) Representative confocal image of a bidirectional iPSC-derived organoid μTENN grown in a 0.5-cm micro-column for 30 DIV and stained for neuronal somata/dendrites (MAP2, green), axons (tau, red), and nuclei (Hoechst, blue). Higher magnification of the organoid cell mass (H) and the neurite region (I) show the morphology of the neurons and the purely axonal nature of the intervening neurites, respectively.

(J) Z stack reconstructions of an ~200-μm-thick cross section of the axonal tract (same μTENN as in G) demonstrate axons distributed within the micro-column lumen as well as at the collagen-agarose border.

Data are presented as mean ± SEM (*$p < 0.05$, **$p < 0.01$, ****$p < 0.0001$; Tukey's multiple comparisons test). Scale bars: 500 μm (A and C), 100 μm (B, D, H, and I), and 200 μm (G).

collagen core by 24 DIV (Figure S2C). To quantify neurite densities, the normalized mean fluorescence intensity of five different regions of interest (ROIs) in the neurite segment was measured (Figures S2A and S2D). This analysis showed that both GFP and Tuj1 intensity ratios were similar in all ROIs that were not immediately adjacent to the organoid cell mass, suggestive of a neurite network that had reached a more homogeneous distribution of neurites by 24 DIV.

At a longer construct length of 1 cm, neurites from each side grew a considerable distance by 24 DIV but had not fully crossed at the center of the neurite segment (Figures 2A and 2B). Continued neurite growth resulted in what appeared to be the formation of a more uniform neurite network by 60 DIV (Figures 2C and 2D). On a qualitative basis, neurite density at the center of the neurite segment increased over time. Individual neurites could be resolved near the center of the μTENN at 24 DIV (Figure 2B), but neurite density increased considerably in the same region by 60 DIV (Figure 2D). To quantify this observation, we again measured normalized mean fluorescence intensities across five ROIs in the neurite segment. At 24 DIV, GFP and Tuj1 intensity ratios progressively decreased from the peripheral to the central parts of the neurite segment (Figures 2E and 2F). At 60 DIV, Tuj1 intensity ratios were similar across all ROIs, and GFP intensity

ratios were similar between the inner and central ROIs. These results suggested active neurite growth and remodeling at 24 DIV and a more homogeneous distribution of neurites at 60 DIV similar to the 24 DIV results for 0.5-cm constructs.

We then used immunohistochemical techniques to characterize the phenotype and distribution of the organoid μTENN neurites. A mixture of axons (tau+) and dendrites (MAP2+) was present in the somatic region (Figures 2G and 2H). However, neurites in the center of the organoid μTENN were exclusively tau+, indicating their axonal nature (Figures 2G and 2I). Z stack reconstructions of the axonal region showed that neurites were distributed throughout the collagen core of the micro-column, although there was a higher density of processes at the collagen-agarose border (Figure 2J).

Somatic Segment Characterization of Bidirectional Organoid μTENNs

Hoechst staining was used to evaluate the migration of organoid cells into the center of the μTENN. We noted slightly more local cell migration at 30 DIV compared with 15 DIV (Figures S3A–S3F). Some nuclei were identified in the center of the μTENN construct, but the number was miniscule compared with the organoid cell mass at either end (Figures S3G and S3H). These data confirmed the relatively strict segregation between the somatic and axonal regions of the organoid μTENN. Notably, the area of Hoechst staining increased substantially between the two time points, which indicated continued growth of the organoid tissue (Figure 3A). Higher magnification examination of the organoid tissue at both time points revealed the formation of cellular aggregates with radial processes, particularly in Tuj1 stains (Figures 3B and S2B). This pattern of cell clustering is not typically seen in conventional organoids but can be encountered in planar and 3D hydrogel cultures of dissociated neurons.

Additional immunohistochemical analysis was performed to examine the cellular composition of the organoid tissue. Astrocytes (GFAP+) were found throughout the somatic segment at both time points (Figures 3C and 3D). Pax6+ cells were also scattered throughout the somatic segment, which indicated the continued presence of progenitor cells at time points greater than differentiation day (dd) 120 (Figure 3E) and explained the growth of the cell mass seen in Figure 3A. Many of the cells within this region stained positive for Tuj1 (Figures 3C and 3D), tau, and MAP2 (Figures 3F and 3G), confirming their neuronal identity.

Neurons positive for Satb2 and CTIP2, which are markers for primarily layer II/III (callosal) and layer V cortical neurons, respectively (Molyneaux et al., 2007), were identified within the organoid tissue, assessed for their spatial distribution, and counted using an automated process (Figure S4). No structural organization could be identified in some cases (Figures 3H and 3J), but some degree of laminar structure was preserved in others (Figures 3I and 3K). Overall, constructs lacking structure were more commonly observed (Figure 3L). However, the frequency of constructs with segregation of Satb2+ and CTIP2+ cells increased from 24 DIV to 60 DIV (Figures 3L and 3M). Co-localization of Satb2 and CTIP2 labeling was observed at both time points (Figure 3N), a finding that has been associated with a distinct subpopulation of cortical projection neurons (Harb et al., 2016). The percentage of CTIP2+ cells also expressing Satb2 decreased from 24 to 60 DIV, which mirrors murine development (Harb et al., 2016; Leone et al., 2015).

Anatomic and Functional Integration between Organoids

To evaluate for integration between the organoids at the two ends of bidirectional organoid μTENN, we analyzed constructs in which one organoid was GFP+ and the other was RFP+. We observed crossing of axons originating from each end at later time points (Figures 4A–4D). We also found instances of axons from one organoid reaching and intermingling with the other organoid at the opposite end of the μTENN (Figures 4E and 4F). There were synaptic puncta present in this region of GFP + processes mixed with RFP + somata (Figure 4G). These data indicate a degree of anatomic integration between the organoids at each end of the μTENN construct.

We next investigated functional connectivity between the organoids in a bidirectional μTENN using Fluo4-based calcium activity (Figure 4H). Shorter constructs were necessary to capture activity from both organoids simultaneously. Spontaneous calcium events in the organoids were observed with an average frequency of 0.073 $\pm$ 0.032 events/s (n = 12, mean $\pm$ standard deviation). Synchronous calcium activity was observed in pairs of neurons, one from each organoid in the construct (Figure 4I). Assessment of

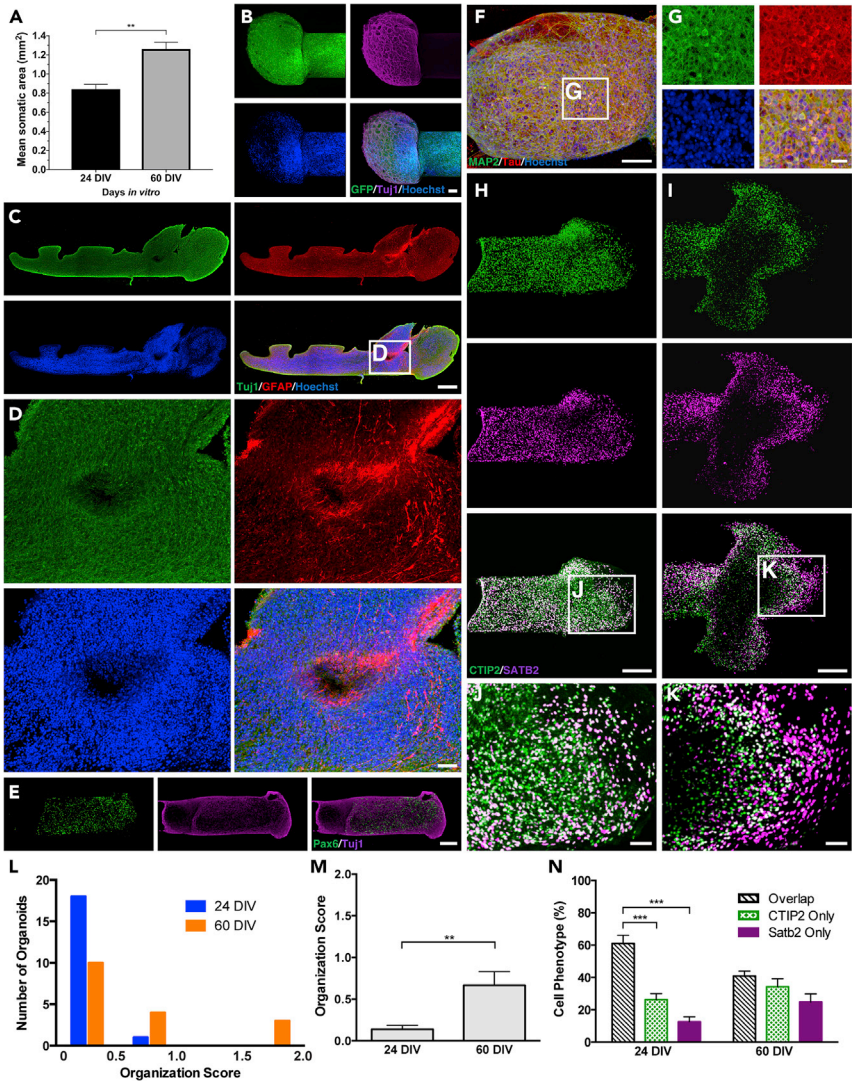

Figure 3. Characterization of the Somatic Segment of the Organoid μTENNs

(A) Quantification of Hoechst staining in 1-cm μTENNs at 24 and 60 DIV demonstrates a significant increase in somatic area as a function of time. Data presented as mean ± SEM (**$p < 0.01$; unpaired t test).

(B) High-magnification image of the organoid cell mass from a 1-cm GFP+ ESC-derived μTENN at 24 DIV stained with Tuj1 (magenta) and Hoechst (blue) shows neuronal clusters connected by neurites in a radial configuration.

(C) Confocal reconstruction of an organoid somatic region in a 1-cm ESC-derived μTENN at 60 DIV stained for Tuj1 (green), GFAP (red), and Hoechst (blue). Astrocytes are scattered throughout the organoid aggregate.

(D) Magnified images of the organoid somatic region showing cellular morphologies.

(E) Pax6+ neural progenitors are found throughout the organoid cell mass (1-cm construct at 24 DIV).

(F) Confocal image of the somatic region of an iPSC-derived organoid μTENN at 15 DIV stained for MAP2 (green), tau (red), and nuclei (Hoechst).

(G) Magnified image of a region in (F) showing examples of neuronal morphology observed within the organoid cell mass.

(H–K) Confocal images of two different ESC-derived μTENN constructs demonstrate the presence of upper- (Satb2, magenta) and lower-layer (CTIP2, green) cortical neurons in the organoid cell mass. Intermixing of these two populations is observed in (H) and (J), whereas some degree of laminar segregation is seen in (I) and (K).

(L) Each side of a cohort of constructs (24 DIV: $n = 11$ constructs/19 available sides, 60 DIV: $n = 10$ constructs/17 available sides) was scored for its degree of structural organization based on the spatial distribution of Sabt2+ and CTIP2+ cells (0 = no organization, 1 = geographic segregation but no laminar structure, 2 = laminar structure). Averaged scores from three blinded authors (D.K.C., W.G., H.I.C.) are depicted as histograms with four bins (≤ 0.5, >0.5 and ≤ 1, >1 and ≤ 1.5, and >1.5 and ≤ 2) for each time point.

(M) The mean of the averaged organization scores for each time point is illustrated.

Figure 3. *Continued*

(N) In the same group of constructs that was analyzed for structure, the frequency of Satb2+, CTIP2+, and Satb2+/CTIP2+ cells was quantified at each time point.

Data in M and N are presented as mean ± SEM (**p < 0.01, ***p < 0.001; M, unpaired t test; N, Tukey's multiple comparisons test). Scale bars: 100 μm (B and F), 300 μm (C), 50 μm (D, J, and K), 150 μm (E), 25 μm (G), and 200 μm (H and I).

multiple pairs of cells showed a high degree of variability in the level of calcium activity synchrony both within an organoid and between organoids (Figure 4J). Looking specifically at synchrony between organoids, 16/36 (0.44) pairs of cells had a synchronization index (SI) greater than 0.5 on a 0–1 scale, and 9/36 (0.25) pairs had an SI greater than 0.8. These results are suggestive of at least some degree of functional connectivity between the two ends of the organoid μTENN.

DISCUSSION

We have produced the first example of constrained, long-projecting cortical axon tracts derived from human stem cell-derived brain organoids. It was recently shown that cortical organoids embedded in agarose extend axonal bundles of different identities (i.e., intracortical versus subcortical projection) into the adjacent hydrogel (Giandomenico et al., 2019). Our constructs, which mirror the architecture of gray and white matter in the brain, build upon this work. The use of precisely engineered hydrogel micro-columns constrains axon growth in a pre-specified direction and facilitates tolerance of the physical manipulations required for transplantation into the brain. This work combines principles from the disciplines of stem cell biology and neural tissue engineering (Yin et al., 2016) and represents a first step toward the possibility of rewiring the brain with patient-specific, laboratory-grown cortical tissue spanned by axon tracts.

Developing methods for repairing axonal injury in the brain is particularly important because of the vital role axons serve in maintaining cerebral network function (Follett et al., 2009; Riley et al., 2011). The approach of generating axon tracts in the laboratory has certain advantages over promoting axon growth *in vivo*, including greater control over cell types, gene expression, and growth conditions (Chen et al., 2016). At the time of transplantation, there is also greater control over which regions of the brain are reconnected. The concept of μTENNs is one example of this approach that permits precise control over the architecture and physical properties of a 3D construct (Cullen et al., 2012; Harris et al., 2016). Previously, it has been demonstrated that μTENNs built from aggregates of dissociated rat embryonic cortical neurons survive, maintain their structure, and project neurites into adjacent brain tissue up to 1 month after stereotactic implantation (Struzyna et al., 2015b). This work recently was expanded to include μTENNs derived from aggregates of dissociated rat ventral mesencephalic (dopaminergic) neurons that were precisely implanted to reconstruct the nigrostriatal pathway in rats (Struzyna et al., 2018). The current work improves upon the translational potential and increases the sophistication of μTENN technology by utilizing brain organoids as the source of neurons and axonal processes. These structured neural tissues can be derived from patient-specific iPSC lines, and they exhibit the architecture and possibly the micro-circuitry of laminar cortex that is lacking in re-aggregated neuron clusters (Birey et al., 2017; Kadoshima et al., 2013; Lancaster et al., 2013; Pasca et al., 2015; Qian et al., 2016).

Several areas of improvement would benefit future iterations of organoid μTENNs. Although we observed segregation of cortical layer-specific markers in some constructs, most showed intermixing of these markers. This lack of structure could result from variability in organoid growth (Quadrato et al., 2017) or organoid manipulation during μTENN generation. Regarding the latter point, we found that the frequency of organized constructs increased over time. One potential explanation for this observation is that the physical disruption caused by organoid manipulation was mitigated in some cases by continued organoid growth, which restored structure through intrinsic programs of self-organization. The lack of or incomplete restoration of structure could be the product of insufficient time or a degree of structural disruption that was too great to overcome. Prior studies have documented that up to 40% of CTIP2+ cells also express Satb2 (Alcamo et al., 2008). We found a higher percentage of CTIP2+ cells co-localizing with Satb2, which could result from differences in species (human versus rodent), time points examined, and choice of antibodies. Improved control of organoid architecture and phenotype will be important for facilitating the creation of custom cortical constructs, such as vertical versus horizontal circuits (Figure 1A).

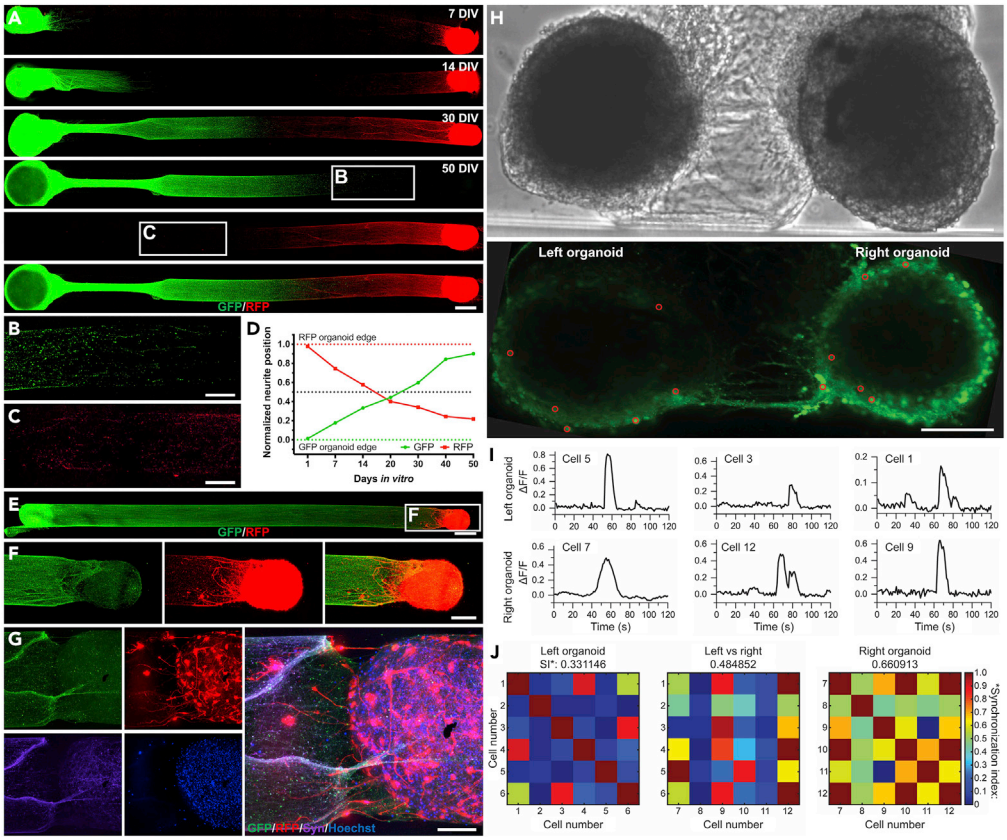

Figure 4. Anatomic and Functional Integration in iPSC-Derived Brain Organoid μTENNs

(A) Bidirectional μTENNs were fabricated with GFP+ and RFP+ organoids on either side in a 1-cm micro-column and imaged over time to observe organoid-specific neurite growth.

(B and C) High-magnification images of the box insets in (A) at 50 DIV show GFP+ (B) and RFP+ (C)_neurites approaching the edge of the opposite organoid. The brightness in these micrographs was increased to visualize the farthest-reaching neurites.

(D) Neurite crossing of the μTENN in (A) was quantitatively analyzed by measuring organoid-specific neurite growth relative to inter-organoid distance as a function of time. A normalized position of 0 and 1 was defined as the edge of the GFP and RFP organoid, respectively. As time progressed, the GFP+ and RFP+ neurites grew closer to the other organoid, respectively.

(E and F) (E) Confocal image of a full-length bidirectional 1-cm μTENN at 60 DIV and (F) high magnification of the RFP+ organoid region show physical intermixing of GFP+ neurites with the RFP+ organoid, suggestive of anatomic integration.

(G) High-magnification image of the RFP+ organoid side of the construct in (E) after staining for synapsin I (purple), showing co-localization of GFP signal with putative pre-synaptic specializations in the RFP+ somatic area.

(H) Calcium activity of hiPSC-derived μTENNs was assessed with bidirectional constructs grown in 1-mm micro-columns to allow simultaneous imaging of both organoids (top, phase contrast; bottom, Fluo-4 fluorescence). Red circles show ROIs chosen for subsequent analysis.

(I) Examples of spontaneous calcium waves from three pairs of cells from the left (top row) and right (bottom row) organoids with synchronized firing.

(J) Synchronization indexes (SIs) were calculated using FluoroSNNAP software. The heatmaps compare the degree of synchronization across different ROIs in the left organoid (left, SI: 0.33), between the two organoids (middle, SI: 0.48), and the right organoid, SI: 0.66). Scale bars: 500 μm (A and E), 250 μm (B, C, and F), and 100 μm (G and H).

Our current protocol for creating human cortical axon tracts 1 cm in length from organoid tissue required 2–3 months for organoid preparation and 1–2 months for axon growth. Generating longer axon lengths in shorter periods of time would be important for human translation. Younger organoids or methods for accelerating organoid maturation (Li et al., 2017) could be used to shorten the time required for organoid preparation. Faster axon growth rates could be attained using growth factor regimens or by adapting other bioengineering techniques, such as axon growth via mechanical stretch (Pfister et al., 2004).

Applications of organoid μTENNs extend beyond reconstructing brain circuitry to serving as physiologically relevant models for studying internodal network function in human neurodevelopment and disease. This 3D system more faithfully replicates the modular structure of the brain than dissociated planar cultures (Shein-Idelson et al., 2011, 2016), and they possess axon tracts that are not found in standard brain organoids. Moreover, organoid μTENNs may be more relevant to human disease than animal models (Lancaster and Knoblich, 2014). Our data demonstrate initial evidence of anatomic and functional integration between the organoids at either end of bidirectional μTENN constructs. Using this platform to study network function will require further examination of the intrinsic neuronal activity of brain organoids (Birey et al., 2017; Quadrato et al., 2017) and a more detailed investigation of the capacity of organoid μTENNs for transmitting data across its axons (Chen et al., 2017). An improved understanding of how activity propagates across organoid μTENNs also would help establish the theoretical efficacy and limitations of using these constructs to restore axonal connectivity *in vivo* in the future.

Limitations of the Study

We derived organoid μTENNs from both an ESC and an iPSC line, but our results may not be completely generalizable to other pluripotent stem cell lines. Maintenance of organoid structure within the μTENNs was examined using a semi-quantitative analysis performed by three independent observers. Future studies could employ quantitative analysis techniques to further improve the rigor of the results. As discussed earlier, additional studies are needed to fully characterize the functionality of the organoid-derived axons. Stimulation and recording experiments will better delineate the connectivity between the two ends of the construct and its capacity to encode and decode information. Other studies are also necessary to empirically validate the value of human brain organoid μTENNs as substrates for *in vivo* brain repair and as platforms for modeling cerebral diseases and disorders.

METHODS

All methods can be found in the accompanying Transparent Methods supplemental file.

SUPPLEMENTAL INFORMATION

Supplemental Information can be found online at https://doi.org/10.1016/j.isci.2019.10.004.

ACKNOWLEDGMENTS

Financial support was provided by the National Institutes of Health (U01-NS094340 [D.K.C.] and T32-NS091006-02S1 [L.A.S.]), Department of Veterans Affairs (Career Development Award #IK2-RX002013 [H.I.C.], VISN4 Competitive Pilot Project Fund [H.I.C.], and Merit Review #I01-BX003748 [D.K.C.]), Michael J. Fox Foundation (Therapeutic Pipeline Program #9998 [D.K.C.]), the Neurosurgery Research and Education Fund (Bagan Family Young Clinician Investigator Award [H.I.C.]), and the National Science Foundation (Graduate Research Fellowship DGE-1845298 [W.J.G.-V.]). The authors thank Oladayo Adewole and Saarang Karandikar for assistance in image acquisition and data analysis, respectively.

AUTHOR CONTRIBUTIONS

Reported data are available upon request. D.K.C. and H.I.C. conceived this project and provided general supervision. D.J. and J.L. maintained stem cell cultures and generated brain organoids. W.J.G.-V. and L.A.S. generated organoid μTENNs. L.A.S., W.J.G.-V., K.L.W., and K.D.B. performed immunohistochemical analysis and/or associated data analysis. All authors contributed to drafting and editing the manuscript.

DECLARATION OF INTERESTS

D.K.C. is a co-founder of two University of Pennsylvania spin-out companies concentrating in applications of neuro-regenerative medicine: INNERVACE, LLC and Axonova Medical, LLC. There are two patent applications related to the methods, composition, and use of micro-tissue engineered neural networks, including U.S. Patent App. 15/032,677 titled "Neuronal replacement and reestablishment of axonal connections" (D.K.C.) and US Patent App. 16/093,036 titled "Implantable living electrodes and methods for use thereof" (D.K.C. and H.I.C.). No other author has a potential conflict of interest to disclose.

Received: November 16, 2018
Revised: June 27, 2019
Accepted: September 30, 2019
Published: November 22, 2019

REFERENCES

Alcamo, E.A., Chirivella, L., Dautzenberg, M., Dobreva, G., Farinas, I., Grosschedl, R., and McConnell, S.K. (2008). Satb2 regulates callosal projection neuron identity in the developing cerebral cortex. Neuron *57*, 364–377.

Bassett, D.S., Khambhati, A.N., and Grafton, S.T. (2017). Emerging frontiers of neuroengineering: a network science of brain connectivity. Annu. Rev. Biomed. Eng. *19*, 327–352.

Birey, F., Andersen, J., Makinson, C.D., Islam, S., Wei, W., Huber, N., Fan, H.C., Metzler, K.R.C., Panagiotakos, G., Thom, N., et al. (2017). Assembly of functionally integrated human forebrain spheroids. Nature *545*, 54–59.

Chen, H.I., Attiah, M., Baltuch, G., Smith, D.H., Hamilton, R.H., and Lucas, T.H. (2014). Harnessing plasticity for the treatment of neurosurgical disorders: an overview. World Neurosurg. *82*, 648–659.

Chen, H.I., Jgamadze, D., Lim, J., Mensah-Brown, K., Wolf, J.A., Mills, J.A., and Smith, D.H. (2019). Functional cortical axon tracts generated from human stem cell-derived neurons. Tissue Eng. Part A *25*, 736–745.

Chen, H.I., Jgamadze, D., Serruya, M.D., Cullen, D.K., Wolf, J.A., and Smith, D.H. (2016). Neural substrate expansion for the restoration of brain function. Front. Syst. Neurosci. *10*, 1.

Chen, H.I., Wolf, J.A., and Smith, D.H. (2017). Multichannel activity propagation across an engineered axon network. J. Neural Eng. *14*, 026016.

Cullen, D.K., Tang-Schomer, M.D., Struzyna, L.A., Patel, A.R., Johnson, V.E., Wolf, J.A., and Smith, D.H. (2012). Microtissue engineered constructs with living axons for targeted nervous system reconstruction. Tissue Eng. Part A *18*, 2280–2289.

David, S., and Aguayo, A.J. (1981). Axonal elongation into peripheral nervous system "bridges" after central nervous system injury in adult rats. Science *214*, 931–933.

Espuny-Camacho, I., Michelsen, K.A., Gall, D., Linaro, D., Hasche, A., Bonnefont, J., Bali, C., Orduz, D., Bilheu, A., Herpoel, A., et al. (2013). Pyramidal neurons derived from human pluripotent stem cells integrate efficiently into mouse brain circuits in vivo. Neuron *77*, 440–456.

Fernandes, K.J., Fan, D.P., Tsui, B.J., Cassar, S.L., and Tetzlaff, W. (1999). Influence of the axotomy to cell body distance in rat rubrospinal and spinal motoneurons: differential regulation of GAP-43, tubulins, and neurofilament-M. J. Comp. Neurol. *414*, 495–510.

Follett, P.L., Roth, C., Follett, D., and Dammann, O. (2009). White matter damage impairs adaptive recovery more than cortical damage in an in silico model of activity-dependent plasticity. J. Child Neurol. *24*, 1205–1211.

Gaillard, A., Prestoz, L., Dumartin, B., Cantereau, A., Morel, F., Roger, M., and Jaber, M. (2007). Reestablishment of damaged adult motor pathways by grafted embryonic cortical neurons. Nat. Neurosci. *10*, 1294–1299.

Giandomenico, S.L., Mierau, S.B., Gibbons, G.M., Wenger, L.M.D., Masullo, L., Sit, T., Sutcliffe, M., Boulanger, J., Tripodi, M., Derivery, E., et al. (2019). Cerebral organoids at the air-liquid interface generate diverse nerve tracts with functional output. Nat. Neurosci. *22*, 669–679.

GrandPre, T., Li, S., and Strittmatter, S.M. (2002). Nogo-66 receptor antagonist peptide promotes axonal regeneration. Nature *417*, 547–551.

Harb, K., Magrinelli, E., Nicolas, C.S., Lukianets, N., Frangeul, L., Pietri, M., Sun, T., Sandoz, G., Grammont, F., Jabaudon, D., et al. (2016). Area-specific development of distinct projection neuron subclasses is regulated by postnatal epigenetic modifications. Elife *5*, e09531.

Harris, J.P., Struzyna, L.A., Murphy, P.L., Adewole, D.O., Kuo, E., and Cullen, D.K. (2016). Advanced biomaterial strategies to transplant preformed micro-tissue engineered neural networks into the brain. J. Neural Eng. *13*, 016019.

He, Z., and Jin, Y. (2016). Intrinsic control of axon regeneration. Neuron *90*, 437–451.

Kadoshima, T., Sakaguchi, H., Nakano, T., Soen, M., Ando, S., Eiraku, M., and Sasai, Y. (2013). Self-organization of axial polarity, inside-out layer pattern, and species-specific progenitor dynamics in human ES cell-derived neocortex. Proc. Natl. Acad. Sci. U S A *110*, 20284–20289.

Lancaster, M.A., and Knoblich, J.A. (2014). Organogenesis in a dish: modeling development and disease using organoid technologies. Science *345*, 1247125.

Lancaster, M.A., Renner, M., Martin, C.A., Wenzel, D., Bicknell, L.S., Hurles, M.E., Homfray, T., Penninger, J.M., Jackson, A.P., and Knoblich, J.A. (2013). Cerebral organoids model human brain development and microcephaly. Nature *501*, 373–379.

Leone, D.P., Heavner, W.E., Ferenczi, E.A., Dobreva, G., Huguenard, J.R., Grosschedl, R., and McConnell, S.K. (2015). Satb2 regulates the differentiation of both callosal and subcerebral projection neurons in the developing cerebral cortex. Cereb. Cortex *25*, 3406–3419.

Li, Y., Muffat, J., Omer, A., Bosch, I., Lancaster, M.A., Sur, M., Gehrke, L., Knoblich, J.A., and Jaenisch, R. (2017). Induction of expansion and folding in human cerebral organoids. Cell Stem Cell *20*, 385–396.e3.

Martinez-Ramos, C., Valles-Lluch, A., Verdugo, J.M., Ribelles, J.L., Barcia Albacar, J.A., Orts, A.B., Soria Lopez, J.M., and Pradas, M.M. (2012). Channeled scaffolds implanted in adult rat brain. J. Biomed. Mater. Res. A *100*, 3276–3286.

Molyneaux, B.J., Arlotta, P., Menezes, J.R., and Macklis, J.D. (2007). Neuronal subtype specification in the cerebral cortex. Nat. Rev. Neurosci. *8*, 427–437.

Pan, L., Alagapan, S., Franca, E., Leondopulos, S.S., DeMarse, T.B., Brewer, G.J., and Wheeler, B.C. (2015). An in vitro method to manipulate the direction and functional strength between neural populations. Front. Neural Circuits *9*, 32.

Pasca, A.M., Sloan, S.A., Clarke, L.E., Tian, Y., Makinson, C.D., Huber, N., Kim, C.H., Park, J.Y., O'Rourke, N.A., Nguyen, K.D., et al. (2015). Functional cortical neurons and astrocytes from human pluripotent stem cells in 3D culture. Nat. Methods *12*, 671–678.

Pfister, B.J., Iwata, A., Meaney, D.F., and Smith, D.H. (2004). Extreme stretch growth of integrated axons. J. Neurosci. *24*, 7978–7983.

Qian, X., Nguyen, H.N., Song, M.M., Hadiono, C., Ogden, S.C., Hammack, C., Yao, B., Hamersky, G.R., Jacob, F., Zhong, C., et al. (2016). Brain-region-specific organoids using mini-bioreactors for modeling ZIKV exposure. Cell *165*, 1238–1254.

Quadrato, G., Nguyen, T., Macosko, E.Z., Sherwood, J.L., Min Yang, S., Berger, D.R., Maria, N., Scholvin, J., Goldman, M., Kinney, J.P., et al. (2017). Cell diversity and network dynamics in photosensitive human brain organoids. Nature *545*, 48–53.

Riley, J.D., Le, V., Der-Yeghiaian, L., See, J., Newton, J.M., Ward, N.S., and Cramer, S.C. (2011). Anatomy of stroke injury predicts gains from therapy. Stroke *42*, 421–426.

Shein-Idelson, M., Ben-Jacob, E., and Hanein, Y. (2011). Engineered neuronal circuits: a new platform for studying the role of modular topology. Front. Neuroeng. *4*, 10.

Shein-Idelson, M., Cohen, G., Ben-Jacob, E., and Hanein, Y. (2016). Modularity induced gating and delays in neuronal networks. PLoS Comput. Biol. *12*, e1004883.

Smith, D.H., Wolf, J.A., Lusardi, T.A., Lee, V.M., and Meaney, D.F. (1999). High tolerance and delayed elastic response of cultured axons to dynamic stretch injury. J. Neurosci. *19*, 4263–4269.

Struzyna, L.A., Browne, K.D., Brodnik, Z.D., Burrell, J.C., Harris, J.P., Chen, H.I., Wolf, J.A., Panzer, K.V., Lim, J., Duda, J.E., et al. (2018). Tissue engineered nigrostriatal pathway for treatment of Parkinson's disease. J. Tissue Eng. Regen. Med. *12*, 1702–1716.

Struzyna, L.A., Harris, J.P., Katiyar, K.S., Chen, H.I., and Cullen, D.K. (2015a). Restoring nervous system structure and function using tissue engineered living scaffolds. Neural Regen. Res. *10*, 679–685.

Struzyna, L.A., Wolf, J.A., Mietus, C.J., Adewole, D.O., Chen, H.I., Smith, D.H., and Cullen, D.K. (2015b). Rebuilding brain circuitry with living micro-tissue engineered neural networks. Tissue Eng. Part A *21*, 2744–2756.

Sun, F., Park, K.K., Belin, S., Wang, D., Lu, T., Chen, G., Zhang, K., Yeung, C., Feng, G., Yankner, B.A., et al. (2011). Sustained axon regeneration induced by co-deletion of PTEN and SOCS3. Nature *480*, 372–375.

Wiessner, C., Bareyre, F.M., Allegrini, P.R., Mir, A.K., Frentzel, S., Zurini, M., Schnell, L., Oertle, T., and Schwab, M.E. (2003). Anti-Nogo-A antibody infusion 24 hours after experimental stroke improved behavioral outcome and corticospinal plasticity in normotensive and spontaneously hypertensive rats. J. Cereb. Blood Flow Metab. *23*, 154–165.

Yin, X., Mead, B.E., Safaee, H., Langer, R., Karp, J.M., and Levy, O. (2016). Engineering stem cell organoids. Cell Stem Cell *18*, 25–38.

Yiu, G., and He, Z. (2006). Glial inhibition of CNS axon regeneration. Nat. Rev. Neurosci. *7*, 617–627.

ISCI, Volume *21*

Supplemental Information

Bundled Three-Dimensional Human Axon Tracts Derived from Brain Organoids

D. Kacy Cullen, Wisberty J. Gordián-Vélez, Laura A. Struzyna, Dennis Jgamadze, James Lim, Kathryn L. Wofford, Kevin D. Browne, and H. Isaac Chen

Supplementary Information

Figures S1-S4

Transparent Methods

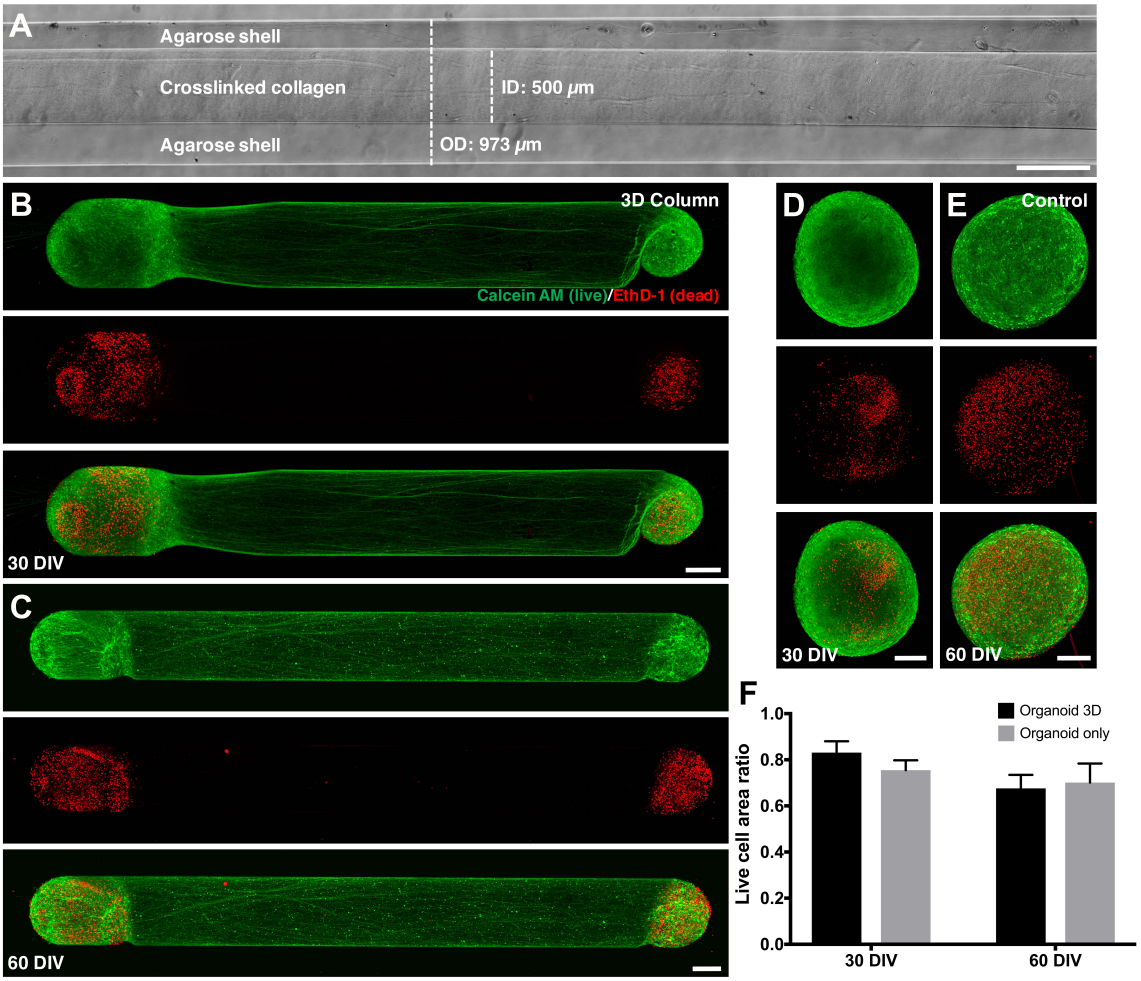

Figure S1. Assessment of cellular viability in organoid µTENNs (related to Figure 1). (A) Phase-contrast image of a micro-column prior to organoid insertion with an outer diameter (OD) and inner diameter (ID) of 973 µm and 500 µm, respectively. The image shows the agarose shell surrounding the inner core composed of crosslinked collagen. Representative confocal reconstructions of bidirectional iPSC-derived organoid µTENNs grown in 0.5-cm micro-columns for 30 (B) and 60 DIV (C) stained for live (calcein AM; green) and dead cells (EthD-1; red). Time-matched organoids floating in media served as controls (D: 30 DIV, E: 60 DIV). (F) There were no significant differences in the live cell

area ratio between 3D and planar cultures over time. Data presented as mean ± SEM. Scale bars: 500 μm (A), 200 μm (B-E).

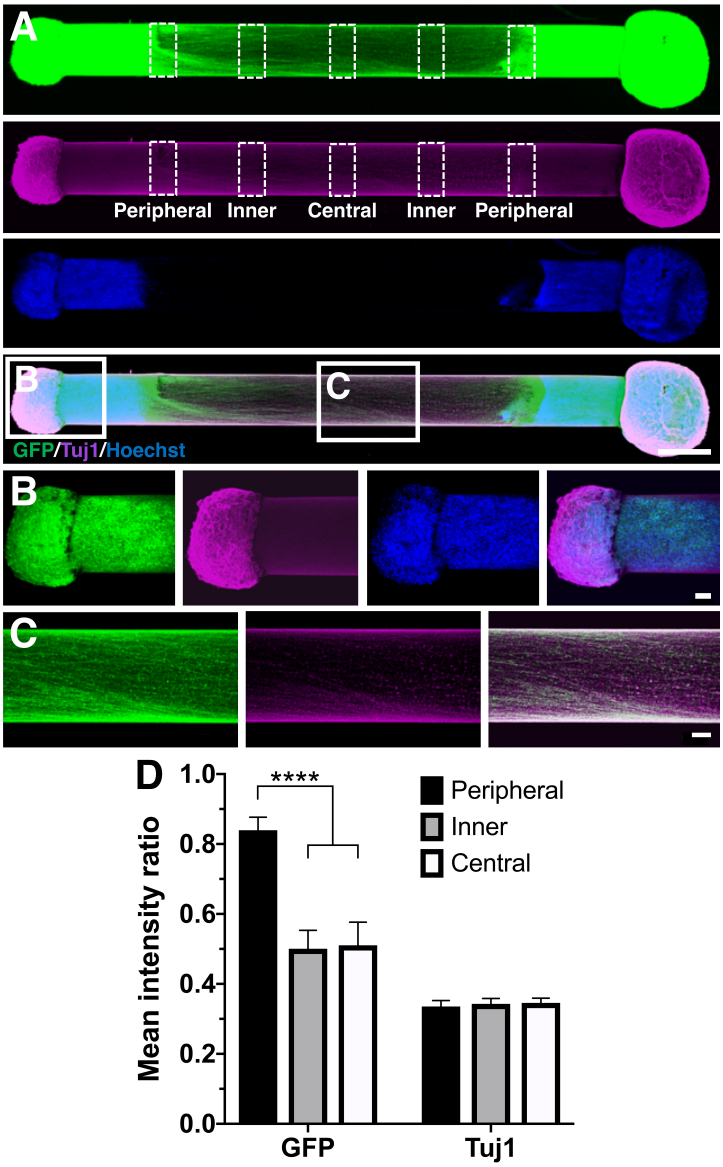

Figure S2. Immunocytochemical analysis of 0.5-cm bidirectional ESC-derived µTENNs (related to Figure 2). (A) Confocal reconstruction of a representative 0.5-cm GFP+ ESC-derived organoid µTENN at 24 DIV stained for Tuj1 (magenta) and Hoechst (blue). There was a distinct separation between regions containing neural somata and neurites. By 24 DIV, neurites had projected across the entire length of the micro-column. Box insets in the merged image of A correspond to higher magnification images of the

organoid cell aggregate (B) and neurites in the central region of the μTENN (C). (D) Neurite outgrowth was quantified as the mean GFP and Tuj1 intensity in five regions of interest (see A) normalized relative to the maximum intensity in the organoid cell mass. Intensity values were statistically similar in the inner and central regions at 24 DIV, demonstrating robust neurite extension across the entire micro-column. Data presented as mean ± SEM (**** $p < 0.0001$; Tukey's multiple comparisons test). Scale bars: 500 μm (A), 100 μm (B-C).

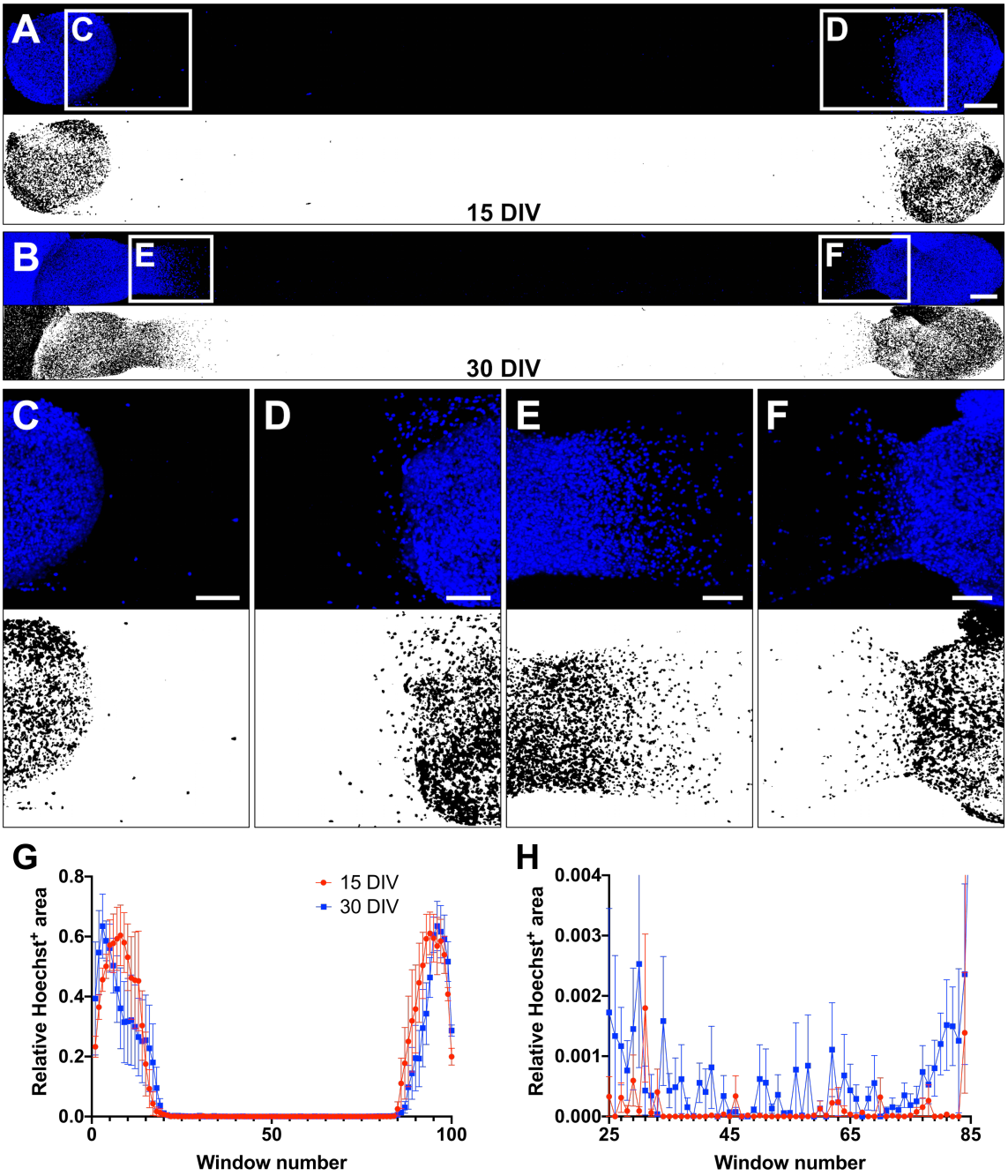

Figure S3. Analysis of cell migration from the organoid mass within micro-columns (related to Figure 3). Bidirectional iPSC-derived organoid µTENNs were cultured for 15 (A) and 30 DIV (B) within 0.5-cm micro-columns, fixed, and stained for nuclei (Hoechst; blue). The binary images of the Hoechst channel are also shown. Higher

magnification images display areas close to the organoid edge in A (C-D) and B (E-F), showing qualitatively a greater degree of local migration at 30 DIV. (G) Cell migration was assessed by measuring the black particle areas (Hoechst+ regions) in the binary images in 100 windows along the length of the construct. The Hoechst+ area was normalized to window size and presented here as a function of window number, where 1 and 100 correspond to the far-left and far-right edges of the Hoechst channel image, respectively. (H) Zoom-in of the graph in G in the region between windows 25 and 85, corresponding to the more central regions of the μTENNs. Data presented as mean ± SEM. Scale bars: 150 μm (A), 200 μm (B), 100 μm (C-F).

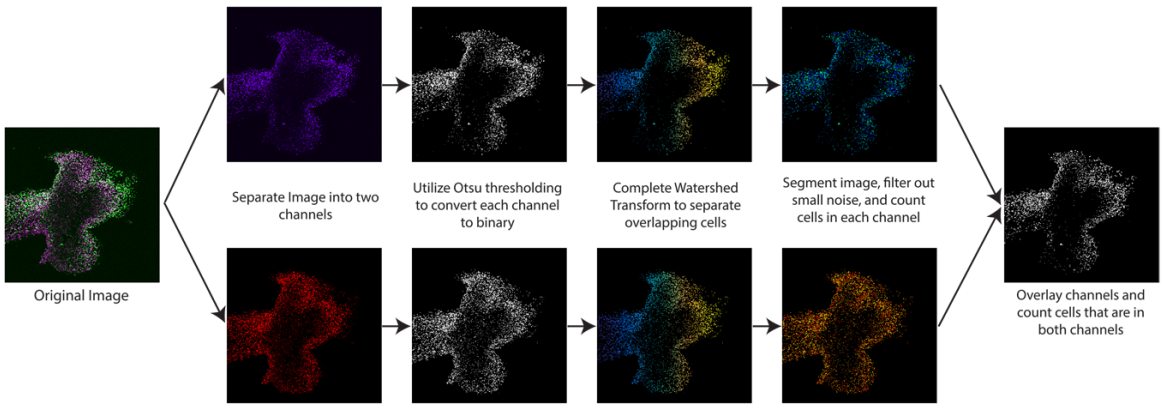

Figure S4. Workflow of automated cell counting (related to Figure 3). Separate color channels were converted to a binary image. A watershed transform was then performed to separate overlapping cells. The resulting image was segmented and filtered to remove noise, and cell counting was performed on this processed image. Combining the processed images for both color channels allowed for counting of the co-labeled cells.

Transparent Methods

Pluripotent stem cell maintenance

The H9 human embryonic stem cell (ESC) line (NIH code WA09; Wicell, Madison, WI) expressing enhanced green fluorescent protein (GFP) driven by the chicken actin promoter (H9-GFP; Children's Hospital of Philadelphia Stem Cell Core, Philadelphia, PA) was generated using zinc finger nucleases to target the expression construct to the AAVS1 locus (Paluru et al., 2014). The C1.2-GFP and C1.2-red fluorescent protein (RFP) lines were created via lentiviral transduction of the C1.2 induced pluripotent stem cell (iPSC) line (BJ-ATCC CRL-2522). All cell lines were maintained on mouse embryonic fibroblast (MEF) feeder cells (CF-1; MTI-Globalstem, Gaithersburg, MD). MEFs were plated one day before passaging at a density of $2x10^5$ cells per well in a 0.1% gelatin-coated 6-well plate (Millipore Sigma, Burlington, MA). Stem cells were cultured in human embryonic stem cell (hES) media containing the following components: DMEM/F12 (Invitrogen, Carlsbad, CA), 20% KnockOut serum replacement (Invitrogen), 1 mM non-essential amino acids (Invitrogen), 1X GlutaMax (Invitrogen), 0.1 mM β-mercaptoethanol (Sigma-Aldrich, St. Louis, MO), 100 U/mL penicillin/100 μg/mL streptomycin (Invitrogen), and 6 ng/mL bFGF (R&D Systems, Minneapolis, MN). Colonies were passaged with TryPLE (Thermo-Fisher, Waltham, MA) or collagenase type IV (Invitrogen) every 7 days. Passage numbers were between 110-135 (H9-GFP) or 20-45 (iPS lines). All cell lines were confirmed to be negative for mycoplasma contamination. Early passage stocks of the cell lines were karyotyped to confirm their genomic integrity (Cell Line Genetics, Madison, WI).

Generation of brain organoids

Brain organoids were generated using a protocol modified from Pasca, et al., 2015. In brief, stem cell colonies were grown until they were approximately 3-4 mm in diameter, after which they were detached by incubation with collagenase type IV for 45-60 minutes at 37^{o}C. The detached colonies were washed once with hES media and then placed in ultra-low attachment 6-well plates (Corning, Corning, NY) in Induction Media consisting of hES media supplemented with 100 nM LDN193189 (Stemgent, Cambridge, MA), 10 µM SB431542 (Stemgent), 2 µM XAV939 (Stemgent), and 10 µM Y-27632 (Tocris Biosciences, Bristol, United Kingdom). From differentiation day (dd) 1-6, the developing embryoid bodies were maintained in Induction Media without Y-27632 with daily media changes. From dd6 onwards, embryoid bodies were cultured on an orbital shaker. From dd6-25, the developing organoids were maintained in Neuronal Media consisting of Neurobasal media (Invitrogen) supplemented with 1:50 B27 without vitamin A (Invitrogen), 1X Glutamax (Invitrogen), 100 U/mL penicillin/100 µg/mL streptomycin (Invitrogen), 20 ng/mL bFGF (R&D Systems), and 20 ng/mL EGF (R&D Systems) with daily media changes until dd17 and then every other day afterwards. From dd25-43, every other day media changes with Neuronal Media supplemented with 20 ng/mL NT3 (R&D Systems) and 20 ng/ML BDNF (R&D Systems) were performed. After dd43, every other day media changes with Neuronal Media without growth factors were performed. Developing iPSC-derived organoids were cut at dd30-35 with sterile fine-tip forceps to a diameter less than 500 µm. Organoids derived from ESC and iPSC cells used for µTENN construction were between dd100-150 and dd62-79, respectively.

Fabrication of micro-column constructs

All materials were obtained from Invitrogen, BD Biosciences, or Sigma-Aldrich unless otherwise noted. The outer hydrogel shell of the micro-columns, which consisted of 1% agarose in Dulbecco's phosphate-buffered saline (DPBS) and had an outer diameter of 973 μm, was generated by drawing the agarose solution into a capillary tube (Drummond Scientific, Broomall, PA) via capillary action. An acupuncture needle (500 μm diameter; Seirin, Weymouth, MA) was inserted into the center of the agarose-filled capillary tube before agarose polymerization to produce space for an inner core. As the micro-columns gelled, a collagen solution was prepared on ice, consisting of 1 mg/mL rat tail type I collagen and the cross-linking agents 11.70 mM N-(3-Dimethylaminopropyl)-N'-ethylcarboimide hydrochloride, 4.3 mM N-Hydroxysuccinimide, and 35.6 mM sodium phosphate monobasic. Afterwards, the needle was removed, and the collagen solution was suctioned into the lumen formed by the needle to fill it completely. The micro-columns with collagen were then incubated at 37ºC for 30 min to allow the collagen to polymerize and cross-link. Finally, the micro-columns were pushed out of the capillary tubes using a 20-gauge needle into DPBS, sterilized under UV light for 30 min, and stored overnight at 37 ºC. The micro-columns then were rinsed twice with warm DPBS to remove remaining traces of the cross-linking agents, transferred to dishes with warm culture media, and then cut to the desired length (1-10 mm).

Organoids derived from ESC cells were cut into small pieces using fine-tip forceps and immediately inserted into one or both ends of the micro-columns under a dissection scope. In some cases, the organoids were subsequently trimmed with forceps to fit fully within the micro-column. Only iPSC-derived organoids that precisely fit

within the micro-column lumen without additional cutting were used in fabricating this type of μTENN. For planar cultures, organoids were plated on tissue culture plates pre-treated with 20 μg/mL poly-d-lysine at room temperature overnight followed by 20 μg/mL laminin at room temperature for 2 hours.

Immunohistochemical analysis of organoid μTENNs

Whole constructs were fixed in 4% formaldehyde for 35 min and permeabilized using 0.3% Triton X-100 (Sigma-Aldrich) plus 4% horse serum (HS; Invitrogen) for 60 min at room temperature. Primary antibodies (see below) diluted in phosphate-buffered saline (PBS, Sigma-Aldrich)/4% HS were applied overnight at 4°C. Appropriate fluorescent secondary antibodies (Alexa-488, -594 and/or -649 [Invitrogen] diluted 1:500 in PBS/4% HS/30 nM Hoechst [Invitrogen]) were applied for 2 hours at room temperature.

Organoid μTENNs were also analyzed using paraffin-embedded sections. Whole constructs were fixed in 4% formaldehyde for 35 min and processed through a 6-hour cycle of ascending concentrations of ethanol and xylene. The constructs were then embedded in paraffin, sectioned at 12 μm, and mounted on Superfrost Plus slides (Thermo-Fisher). Sections were dewaxed through 2 changes of xylene and rehydrated through 2 changes of 100% ethanol, 2 changes of 95% ethanol, and distilled water. For identification of neurons (Tuj-1, MAP2), astrocytes (GFAP), and neural progenitors (Pax6), sections were subjected to modified pressure-cooker/microwave antigen retrieval using TRIS-EDTA buffer for 8 min. Following antigen retrieval, sections were blocked for 30 minutes using blocking serum from the Vectastain Elite Universal Kit (Vector

Labs, PK-6200) in Optimax Wash Buffer (Biogenex, HK583-5K). For identification of layer-specific markers (CTIP2, Satb2), sections were dewaxed and rehydrated as above. They were then subjected to antigen retrieval using 10 mM sodium citrate buffer (pH 6.0) for 30 min at 100 ºC. Sections were cooled and blocked with 5% HS in Optimax Wash Buffer for 30 minutes. Primary antibodies diluted in PBS/4% HS (see below) were applied overnight at 4 ºC. The slides were then washed 3 x 5 minutes in PBS/TWEEN (Sigma), and secondary antibodies (1:500 in PBS/4% HS/30 nM Hoechst) were applied for 1 hour at room temperature. Slides were washed 3 x 5 min with PBS/TWEEN prior to coverslipping with Fluoromount G.

Primary antibodies include Tuj-1 (Sigma T8578, mouse, 1:750), tau (Dako A0024, rabbit, 1:500), MAP2 (Abcam 53992, chicken, 1:1000), MAP2 (Abcam ab11267, mouse, 1:1000), GFAP (Millipore MAB5804, rabbit, 1:500), synapsin I (Synaptic Systems 106-001, mouse, 1:1000), Satb2 (Abcam ab51502, mouse, 1:100), CTIP2 (Abcam ab18465, rat, 1:200), Pax6 (Biolegend 901301, rabbit, 1:100), human nuclear antigen (Millipore MAB1281, mouse, 1:1000).

Imaging

Whole, non-sectioned constructs were imaged with phase-contrast and epifluorescence microscopy using a Nikon Eclipse Ti-S microscope. Images were acquired using an QiClick camera interfaced with NiS Elements software (Nikon). Confocal microscopy was performed on non-sectioned and sectioned constructs using an A1RSI laser scanning confocal microscope (Nikon). Confocal images were reconstructed from full thickness z-stacks. To obtain transverse cross-sections of the axonal tract region

in immunostained μTENNs, constructs were placed vertically in a block of 5% agarose with a preformed orifice that fit the micro-column. The construct was then imaged using a 16x immersion objective and a Nikon A1RMP+ multi-photon microscope linked with NiS Elements AR 4.60.00.

Neurite outgrowth quantification

The length of neurite outgrowth in organoid μTENNs was determined by measuring the distance from the organoid cell mass to the longest observable neurite using Fiji (NIH) in confocal images taken from live constructs at 1, 4, 7, 10, 30, 40, and 50 DIV (n = 4 for all time points except for n = 6 at 30, 40, 50 DIV). GFP+ organoids from the same differentiation batch also were cultured on laminin-coated planar surfaces as controls. In this case, the length of growth was quantified by tracing the length of the longest neurite from phase contrast images taken at 1, 4, 7, 10, and 30 DIV using the Simple Neurite Tracer plugin (n = 9 at all time points except n = 3 at 30 DIV because of organoid detachment). Imaging and quantification of controls stopped after 30 DIV because all organoids had detached. The length change rate at each time point was estimated based on the previous time point by the backward difference method. Differences in outgrowth and growth rate between time points in 3D micro-columns and between planar controls and 3D micro-columns were assessed with one-way analysis of variance (ANOVA) and two-way ANOVA, respectively, with Tukey's test for multiple comparisons ($p < 0.05$ as the criterion for statistical significance). These analyses, and all below unless otherwise noted, were carried out in Prism 8 (GraphPad).

Neurite density quantification

To compare the neurite density along micro-columns, five regions of interest (ROI) of equal size (163 pixels x 80 pixels) were selected in the GFP and Tuj1 channels along the region spanned by axon tracts (n = 3 constructs for each group) in ESC-derived organoid µTENNs. Two peripheral ROIs were chosen adjacent to the organoid cell mass, two inner ROIs were selected with their center at 25 and 75% of the length of the neurite region, and one central ROI was located midway along the neurite region. The ROIs were cropped and converted to 8-bit images using ImageJ (NIH), and the mean gray scale value was measured. These values were corrected for background fluorescence by subtracting the mean gray scale values derived from three randomly selected background regions (163 pixels x 80 pixels) in the original images. To facilitate comparisons across samples, these background-corrected values were normalized relative to the maximum gray scale value in the organoid cell mass region of each sample. Normalized values were averaged across each ROI group (n = 6 for peripheral and inner and n = 3 for central ROIs). Pairwise differences were evaluated with Tukey's test for multiple comparisons ($p < 0.05$ as the threshold for statistical significance).

Assessment of organoid cell mass size

ImageJ was used to measure the area of the organoid cell mass in the Hoechst channel in whole hESC-derived organoid µTENNs. These values were averaged across samples from each group. An unpaired t-test was applied to compare the somatic size between conditions ($p < 0.05$ as the threshold for statistical significance).

Automated Satb2+ and CTIP2+ cell counting

Counting of Satb2+ and CTIP2+ cells in ESC-derived organoid µTENN sections was performed utilizing a custom MATLAB script. This automated, feature-based segmentation methodology was comprised of the following sequential steps (Figure S4). Color images (Satb2 or CTIP2) were converted to a greyscale binary image using Otsu's thresholding. In regions of high cell density, the binary mask represented overlapping cells as connected components, which would result in undercounting of cells. In order to correct for overlapping cells, the binary images were pre-processed with a distance transform gradient, and a watershed transform was then applied to separate clustered cells. Following the watershed transform, individual cells were segmented and counted to generate the number of Satb2+ and CTIP2+ cells. To count the number of Satb2+/CTIP2+ cells, segmented Satb2 and CTIP2 images were overlaid on top of each other. Object coordinates that were positive for both signals were preserved while image coordinates with one or no signals were eliminated. The remaining segmented components represented cells that were double-positive and were quantified. The number of double-positive cells was subtracted from the Satb2 and CTIP2 cell counts to compute the number of Satb2-only and CTIP2-only cells, respectively.

Characterization of organoid tissue structure

The degree of organoid tissue structure in ES-derived organoid µTENN sections was scored using a 0-2 scale (0=no organization, 1=geographic segregation of Satb2+ and CTIP2+ cells but no laminar structure, 2=laminar structure) by three authors (DKC, WG, HIC) who were blinded to the other authors' scores. Mean organization scores were then

calculated. These scores were used to compare sides within organoid μTENN constructs over time. Organization scores were compared across time points with an unpaired *t* test. Data segregated by organization classification and time points were analyzed with a two-way ANOVA. Frequency of cellular phenotypes was compared across phenotype and time points using two-way ANOVAs. If differences were detected between groups, Tukey's post hoc test was employed with a Bonferroni correction to account for multiple comparisons ($p < 0.05$ was considered significant). All analyses were carried out in R Studio Version 1.0.143.

Analysis of neuronal migration

The extent of neuronal migration from the organoid mass within μTENNs was evaluated using bidirectional iPSC-derived brain organoid μTENNs cultured for 15 and 30 DIV ($n = 4$ each) within 0.5-cm micro-columns. After incubation of fixed constructs for 10 min with Hoechst (1/10,000 in PBS), these μTENNs were imaged, and the Hoechst channel was analyzed for cell migration. First, binary masks of the images were made in Fiji and precisely cropped to encompass only the width of the lumen and the distance from organoid to organoid. The Hoechst+ area was measured in 100 windows of equal width along this distance and normalized relative to the window area using a custom-made MATLAB script. Differences between normalized Hoechst+ areas as a function of window number and time were assessed with two-way ANOVA and Sidak's multiple comparisons test ($p < 0.05$ was significant).

Viability quantification

We assessed viability in hiPSC-derived organoids at 30 and 60 DIV using bidirectional μTENNs (n = 6 constructs at each time point) and controls consisting of organoids cultured floating in media (n = 7 at each time point). Organoid μTENNs and controls were rinsed once in DPBS and incubated in 1/2000 calcein-AM and 1/500 ethidium homodimer-1 (EthD-1) (ThermoFisher) in DPBS for 30 min at 37ºC. After two rinses in DPBS, whole constructs and controls were imaged using confocal microscopy, and the maximum intensity projection of the z-stacks was taken. To estimate viability within the organoid mass, the green (calcein-AM+) and red (EthD-1+) channels of the projection were converted to 8-bit images using Fiji. Subsequently, the images were binarized by setting manual global thresholds to obtain cell-shaped regions; different thresholds were chosen for each image given that consistent values did not accurately reflect intrinsic differences in each image. The areas of calcein AM+ and EthD-1+ cells were quantified only in the organoid mass region, and the live cell area ratio was defined as the ratio of calcein AM+ area over the total area of calcein AM+ and EthD-1+ cells. Differences in viability in terms of time and group were analyzed using two-way ANOVA with Tukey's test for multiple comparisons ($p < 0.05$ was considered significant).

Analysis of organoid integration and calcium signaling

Bidirectional μTENNs were fabricated with a GFP+ and RFP+ organoid on either end of a 1-mm micro-column. These constructs were imaged with confocal microscopy at different time points, and the distances between the longest GFP+ and RFP+ neurite and the edge of the GFP+ and RFP+ organoid were measured. To approximate the time for

differential neurite crossing and integration with the other organoid mass, the normalized neurite position was defined as the organoid-specific (GFP+ or RFP+) neurite length relative to the distance between the two organoids. With this definition, 0 and 1 referred to the edges of the GFP+ and RFP+ organoid, respectively.

Calcium activity was assessed after culturing iPSC-derived, non-fluorescent, bidirectional organoid μTENNs for 15 DIV (dd77 at imaging) in a 1-mm micro-column. The constructs were incubated with 5 μM Fluo-4 (Thermo Fisher Scientific) in Neuronal Media without growth factors for 30 min at 37°C and then rinsed with media before imaging. Calcium imaging was performed in Neuronal Media at room temperature using a 10x objective and Nikon A1RMP+ multi-photon microscope paired with NiS Elements AR 4.60.00. Videos were recorded at 5 frames per second.

Selection of ROIs and extraction of mean gray values were performed using ImageJ. Calcium responses were calculated using Fluoro-SNNAP software. In brief, background was subtracted from the signals in each sample, and then, $\Delta F/F0$ values were calculated for each ROI using the 10th percentile value of the complete raw fluorescence trace as *F0*. Identification of calcium events and calculation of synchronization indices (scale of 0–1) within and between organoids were also done with FluoroSNNAP. For each sample, 6 ROIs around active neuronal somata were selected for these analyses. Default FluoroSNNAP settings, including the reference calcium waveform library, were used.